

# Vector mechanics-based simulation of large deformation behavior in RC shear walls using planar four-node elements

Hongmei Zhang<sup>1a</sup>, Yufei Shan<sup>2,b</sup>, Yuanfeng Duan<sup>\*1</sup>, Chung Bang Yun<sup>1,c</sup> and Song Liu<sup>2,d</sup>

<sup>1</sup>College of Civil Engineering and Architecture, Zhejiang University, 866, Yuhangtang Road, Hangzhou, 310058, China

<sup>2</sup>Department of Disaster Mitigation for Structures, Tongji University, 1239, Siping Road, Shanghai, 200092, China

(Received September 13, 2018, Revised August 9, 2019, Accepted August 26, 2019)

**Abstract.** For the large deformation of shear walls under vertical and horizontal loads, there are difficulties in obtaining accurate simulation results using the response analysis method, even with fine mesh elements. Furthermore, concrete material nonlinearity, stiffness degradation, concrete cracking and crushing, and steel bar damage may occur during the large deformation of reinforced concrete (RC) shear walls. Matrix operations that are involved in nonlinear analysis using the traditional finite-element method (FEM) may also result in flaws, and may thus lead to serious errors. To solve these problems, a planar four-node element was developed based on vector mechanics. Owing to particle-based formulation along the path element, the method does not require repeated constructions of a global stiffness matrix for the nonlinear behavior of the structure. The nonlinear concrete constitutive model and bilinear steel material model are integrated with the developed element, to ensure that large deformation and damage behavior can be addressed. For verification, simulation analyses were performed to obtain experimental results on an RC shear wall subjected to a monotonically increasing lateral load with a constant vertical load. To appropriately evaluate the parameters, investigations were conducted on the loading speed, meshing dimension, and the damping factor, because vector mechanics is based on the equation of motion. The static problem was then verified to obtain a stable solution by employing a balanced equation of motion. Using the parameters obtained, the simulated pushover response, including the bearing capacity, deformation ability, curvature development, and energy dissipation, were found to be in accordance with the experimental observation. This study demonstrated the potential of the developed planar element for simulating the entire process of large deformation and damage behavior in RC shear walls.

**Keywords:** vector mechanics; planar element; large deflection; nonlinear analysis; RC shear walls

## 1. Introduction

The seismic performance evaluation of reinforced concrete (RC) shear wall structures and the application of the displacement-based seismic design method are based on accurate simulations of structural responses (Thomsen and Wallace 2004, Zhang *et al.* 2014). However, computational stability, accuracy, and convergence continue to represent significant challenges when simulating the large deformation behavior of RC shear walls.

As an anisotropic composite material, concrete exhibits cracking and crushing behaviors, which make the failure analysis complex, especially at the large deformation stage when RC shear walls are subjected to vertical and horizontal loads. Few simulation methods have successfully analyzed the nonlinear behaviors of various types of RC structural elements under various stress combinations

(Ayoub and Filippou 1998). Traditional finite-element algorithms assume the shape functions of the deformations, which should satisfy the continuity condition. Variations based on the global coordinates may induce a non-equilibrium condition among the forces when applying traditional finite-element method (FEM) (Messaoudi *et al.* 2018 and Gulsan *et al.* 2018). Furthermore, the calculations of stress and strain depend on the deformation, and large deformations may cause numerical instabilities when calculating the internal forces. During the stiffness descending stage, an ill-conditioned stiffness matrix and complex differential equation may also prevent the computation from converging, or may require a large computation time. Moreover, the superposition of a small deformation on a large rigid body motion for the traditional FEM is not suitable for the damage process. The foundation of the continuum mechanics theory and the complexity of the force-deformation mechanism of the shear wall present great challenges for the simulation of the large deformation and large motion problem (Zhang *et al.* 2010b).

In case of the ordinary quadratic four-node elements used in the analysis of the large deformation and damage development process, small deformation calculation assumption, error accumulation, and integration for the stiffness may cause serious errors. Furthermore, for the traditional four-node element, especially with a complete linear form, there will be a “shear lock” problem in the shear and bending interaction behavior, which also causes considerable errors, even with a fine mesh size.

\*Corresponding author, Professor

E-mail: [ceyfduan@zju.edu.cn](mailto:ceyfduan@zju.edu.cn)

<sup>a</sup> Associate Professor

E-mail: [zhanghongmei@zju.edu.cn](mailto:zhanghongmei@zju.edu.cn)

<sup>b</sup> M.Sc. Student

<sup>c</sup> Professor

E-mail: [ycb@zju.edu.cn](mailto:ycb@zju.edu.cn)

<sup>d</sup> M.Sc. Student

The vector mechanics was developed based on Newton's law, and it aimed to solve large deformation, fragmentation, and collapse problems (Ting *et al.* 2004a, b, 2012, Shih *et al.* 2004). In vector mechanics, the structure is simulated as an assembly of mass particles, and a superposition method of the incremental response is applied to simulate the nonlinear response by increasing the time step. In this way, the assembly of the global stiffness matrix is not required, and the ill-conditioned stiffness matrix that induced instability in the calculation can be avoided. Based on the theory of vector mechanics, computation procedure, Vector Form Intrinsic Finite Element (VFIFE) method has been developed (Ting, et. al. 2004a, 2012). Wu *et al.* (2006) proposed a plane element of VFIFE and carried out a large deflection analysis for flexible frame structures. Wu (2008) developed a quadrilateral membrane element of VFIFE and verified the approach by performing a large deflection analysis of membrane structures. Wang *et al.* (2011) tested a VFIFE planar element for an elasto-plastic plane frame under static and dynamic loads. Wu (2013) performed a dynamic nonlinear analysis of shell structures. Luo (2009a, b) developed vector mechanics-based theory for the large deflection analysis of deployable structures, bar assemblies, and membranes (Luo and Yang 2014, Yang *et al.* 2014). A vector mechanics-based solution to the cracking problem has also been reported with fairly good results (Duan *et al.* 2017). Duan *et al.* (2014) developed the vector mechanics to simulate the entire process of the collapse for a cable-stayed bridge under earthquake load, which presents a successful study in collapse simulation.

Vector mechanics has advantages in the solving of large deformation, deflection, and fracture problems compared with the traditional continuum mechanics. For the large response simulations of RC shear walls, concrete cracking, concrete crushing and steel bar damage will induce fracture problems and may cause the simulation results to be inaccurate and unstable (Ting *et al.* 2004a, b). The deformation coordination is essential before the vector mechanics-based four-node planar element application, as well as the particle position, which can be obtained by solving the differential equation. Furthermore, the fluctuation problem caused by the loading speed when applying dynamic equilibrium function needs to be eliminated. When dealing with a static problem, the loading speed, mesh dimension, and damping factor will also induce errors in the simulation accuracy.

This study aims to develop an efficient framework for large deformation and damage involved simulations using precisely described concrete material properties for RC shear walls or this kind of planar problem. The following perspectives are involved: (i) The development of a vector mechanics-based planar four-node element subjected to large deformation; (ii) Damage criteria involving the biaxial concrete constitutive model corresponding to the vector mechanics-based four-node planar element considering concrete cracking and crushing. (iii) The treatment of the loading speed, mesh size, and damping factor for the static response use existing vector mechanics, which was developed for dynamic response analysis. The proposed simulation framework the developed four-node element has

been verified based on a group of laboratory test results on RC shear walls.

## 2. Four-node planar element

### 2.1 Kinematics equation

According to the present vector mechanics, structural systems are supposed to be constituted by particles and elements, and the mass is concentrated on the particles (Ting *et al.* 2004a, Shih *et al.* 2004). The equations of motion of the particle are established according to D'Alembert's principle, and the internal force of each particle is calculated using the path element. The equation of motion of particles under both internal and external forces satisfies Newton's law, which can be shown as:

$$m \frac{d^2 x}{dt^2} = P_{ext} + P_{int} + P_d \quad (1)$$

where  $m$  is the mass matrix, which can be discrete as separate particles according to the body dimension and density;  $x$  is the position vector;  $t$  is the time variable;  $P_{ext}$  is the external force vector;  $P_{int}$  is the internal force vector caused by the neighboring elements; and  $P_d$  is the damping force vector.

The path element and time steps are used to describe the motion of particles by solving Eq. (1). The path element is the segmented movement of particles along the path of motion. The time step is the minimum unit in the integral. One or multiple time steps can be included into one path element. The massive particle motion is continuous and has the same characters in the path element. The material property transform only occurs at the joint path element, e.g., the critical turning point of the concrete for cracking or crushing. By controlling the length of time steps, the structural deformation can be divided into small fragments to satisfy the small deflection assumption of material mechanics.

By applying the central differential method, Eq. (1) can be converted into the following explicit form (Ting, Duan, and Wu 2012):

$$x^{n+1} = c_1 h^2 m^{-1} (P_{ext} + P_{int}) + 2c_1 x^n - c_2 x^{n-1} \quad (2)$$

where  $c_1 = 1/(1 + 0.5\xi h)$ ,  $c_2 = (1 - 0.5\xi h) * c_1$ ;  $\xi$  is the damping factor;  $h$  is the length of the time step;  $x^{(n+1)}$ ,  $x^{(n)}$ , and  $x^{(n-1)}$  are the position vectors at the time steps of  $(n+1)$ ,  $n$ , and  $(n-1)$ , respectively.

As shown in Eq. (2), the errors in the displacement ( $x$ ) of the particles are caused by the time step and the damping factor. If the velocity is zero, the method becomes the Ritz approach, and there will be no convergence problem. However, in real cases, the loading process is not a real static process; there is a damping force that is caused by the loading speed. The damping effect of a quasi-static process can be eliminated by a very low loading speed, and the damping factor is also assumed to be a large value in order to eliminate the possible vibration for a static problem. The impacts of loading speed and damping factor on simulating a static problem of RC shear walls are also discussed in this

study.

## 2.2 Transformation of displacement vector and shape function

As stated above, the time sequence and superposition are adopted in vector mechanics (Ting, 2004a). The increasing nodal displacement vector  $\Delta\eta_i$  from time  $t_n$  to time  $t_{n+1}$  in global coordinates can be represented by the position transformation as follows:

$$\Delta\eta_i = x_i^{n+1} - x_i^n = \{u_i, v_i\}^T, i = 1, 2, 3, 4 \quad (3)$$

where  $x_i^n$  and  $x_i^{n+1}$  are position vectors of node  $i$  at times  $t_n$  and  $t_{n+1}$ , respectively; and  $i = 1, 2, 3$ , and  $4$  is defined as the node number of the four-node planar element.

The plane object being analyzed can be divided into individual elements according to the simulation demands in order to compute the internal forces independently. The element model is a continuum that satisfies the requirements of the continuity. The masses are concentrated at the four nodes. For the four-node planar element, the displacement vector  $u_e$  can be expressed as

$$u_e = \{u_1, v_1, u_2, v_2, u_3, v_3, u_4, v_4\}^T \quad (4)$$

The transformation between the global and local coordinates are shown as:

$$\Delta\hat{\eta}_i = \begin{Bmatrix} \hat{u}_i \\ \hat{v}_i \end{Bmatrix} = \Omega \begin{Bmatrix} u_i \\ v_i \end{Bmatrix} \quad (5)$$

Here,  $\Delta\hat{\eta}_i$  is the displacement vector  $(\hat{u}_i, \hat{v}_i)$  of node  $i$  in the local coordinate.  $(\hat{u}_i, \hat{v}_i)$  and  $(u_i, v_i)$  are the horizontal and vertical displacement vectors in the local and global coordinate, respectively.  $\Omega$  is the transform matrix from the global coordinate to the local coordinate.

A local coordinate system for a deformed element is established in order to reduce the number of degrees of freedom of the elements. Setting the reference point located at node 1, we get

$$\hat{x}_1 = \hat{y}_1 = 0 \quad (6)$$

The  $\hat{x}$ -axis of the local coordination can be set to be parallel to the nodal displacement vector  $(\Delta\hat{\eta}_2)$  at node 2, as shown in Fig. 1. Accordingly, the three displacement variables are zero:

$$\hat{u}_1 = \hat{v}_1 = \hat{v}_2 = 0 \quad (7)$$

The transformation matrix for deformation coordinates  $\Omega$  in Eq.5 can be obtained using the geometrical relationship (Ting et al. 2004b), as shown in Fig. 1 as

$$\Omega = \begin{bmatrix} \hat{e}_x \\ \hat{e}_y \end{bmatrix} = \frac{1}{|\Delta\eta_2|} \begin{bmatrix} \Delta\eta_{2x} & \Delta\eta_{2y} \\ -\Delta\eta_{2y} & \Delta\eta_{2x} \end{bmatrix} \quad (8)$$

where  $\hat{e}_x$  and  $\hat{e}_y$  are the direction unit vectors in the  $x$  and  $y$  directions of local coordinate  $\hat{e}_x = \frac{1}{|\Delta\eta_2|} \{\Delta\eta_{2x}, \Delta\eta_{2y}\}$ ;  $\hat{e}_y = \frac{1}{|\Delta\eta_2|} \{-\Delta\eta_{2y}, \Delta\eta_{2x}\}$ , which is

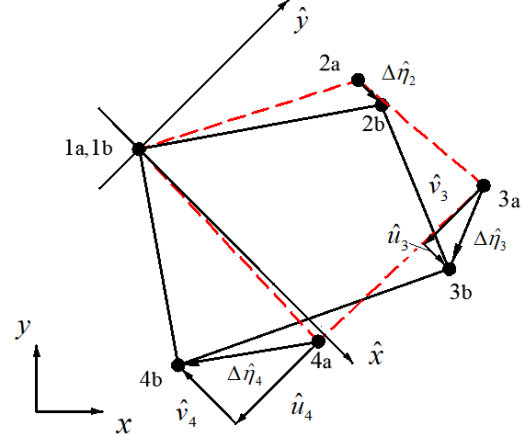


Fig. 1 Local coordinates of a deformed element

Note: The planer element moves from a (1a, 2a, 3a, 4a) to b (1b, 2b, 3b, 4b) in the deformation process.

perpendicular to  $\hat{e}_x$ ;  $\Delta\eta_2 = \{\Delta\eta_{2x}, \Delta\eta_{2y}\}^T$  is the displacement vector of node 2 in the global coordinate system.

To find the state of any point in the element, the shape function ( $N_i$ ) is employed.  $N_i$  is used to transfer the nodal displacement to that of any point in the element, as described by Eqs. (9) and (10):

$$\hat{x} = \sum_{j=1}^n N_j(s, t) \hat{x}_j, \quad i = 1, 2, 3, 4; n = 4 \quad (9)$$

$$\Delta\hat{\eta} = \sum_{j=1}^n N_j(s, t) \Delta\hat{\eta}_j, \quad i = 1, 2, 3, 4; n = 4 \quad (10)$$

where  $(s, t)$  is the computed point of the local coordinate and  $(\hat{x}, \hat{y})$  is the local position (Ting et al. 2004b). The shape functions for each node can be written as

$$\begin{aligned} N_1(s, t) &= \frac{(1-s)(1-t)}{4} & N_2(s, t) &= \frac{(1+s)(1+t)}{4} \\ N_3(s, t) &= \frac{(1+s)(1-t)}{4} & N_4(s, t) &= \frac{(1-s)(1+t)}{4} \end{aligned} \quad (11)$$

## 2.3 Strain and stress transfer Matrix

As described above, there are five independent variables for the four-node planar element in the local coordinates:

$$\hat{u}_e = \{\hat{u}_2, \hat{u}_3, \hat{v}_3, \hat{u}_4, \hat{v}_4\}^T \quad (12)$$

The incremental strain  $d\hat{\epsilon}$  is obtained by using the method that is similar to the traditional FEM (Ting et al. 2004b):

$$d\hat{\epsilon} = \{d\hat{\epsilon}_x, d\hat{\epsilon}_y, d\hat{\gamma}_{xy}\}^T = B\hat{u}_e \quad (13)$$

where  $B$  is the geometry matrix

$$B = \frac{1}{J} \{B_2, B_3, B_4\}_{3 \times 5} \quad (14)$$

$$B_2 = \begin{bmatrix} \hat{y}_t N_{2,s} - \hat{y}_s N_{2,t} \\ 0 \\ \hat{x}_s N_{2,t} - \hat{x}_t N_{2,s} \end{bmatrix} \quad (15)$$

$$B_i = \begin{bmatrix} \hat{y}_t N_{i,s} - \hat{y}_s N_{i,t} & 0 \\ 0 & \hat{x}_s N_{i,t} - \hat{x}_t N_{i,s} \\ \hat{x}_s N_{i,t} - \hat{x}_t N_{i,s} & \hat{y}_t N_{i,s} - \hat{y}_s N_{i,t} \end{bmatrix} \quad i=3, 4 \quad (16)$$

where,  $\hat{x}_s, \hat{x}_t, \hat{y}_s$ , and  $\hat{y}_t$  represent the derivative  $\partial \hat{x} / \partial s$ ,  $\partial \hat{x} / \partial t$ ,  $\partial \hat{y} / \partial s$ , and  $\partial \hat{y} / \partial t$ , respectively, and

$$N_{i,s} = \partial N_i / \partial s, \quad N_{i,t} = \partial N_i / \partial t \quad (17)$$

$$\hat{x}_s = \sum_{j=2}^4 N_{j,s} \hat{x}_j, \quad \hat{x}_t = \sum_{j=2}^4 N_{j,t} \hat{x}_j \quad (18)$$

$$\hat{y}_s = \sum_{j=2}^4 N_{j,s} \hat{y}_j, \quad \hat{y}_t = \sum_{j=2}^4 N_{j,t} \hat{y}_j \quad (19)$$

The Jacobian matrix in Eq. (14) is shown below as

$$J = \det \begin{vmatrix} \hat{x}_s & \hat{y}_s \\ \hat{x}_t & \hat{y}_t \end{vmatrix} \quad (20)$$

For cases involving the four-node planar element, the above variables are confirmed value after the derivation. The stress incremental vector  $d\hat{\sigma}$  is the variable of the incremental strain  $d\hat{\varepsilon}$  and element modulus matrix of  $E$ . Then, the incremental stress can be expressed as

$$d\hat{\sigma} = E d\hat{\varepsilon} = E B \hat{u}_e \quad (21)$$

## 2.4 Virtual work and internal force

The virtual work principle is applied to resolve the internal force of the elements at time step  $t_{n+1}$  in Eqs. (22) and (23) as:

$$W_{\text{out}} = W_{\text{in}} \quad (22)$$

$$\sum_{i=1}^4 \hat{f}_{n+1}^i \cdot \hat{u}_{n+1}^i = \hat{d} \cdot \hat{u}_{n+1}^i \int_{\hat{A}} \hat{B}^T \hat{\sigma}_{n+1} d\hat{A} \quad (23)$$

where  $\hat{d}$  and  $\hat{A}$  represent the thickness and area of the element, respectively, and

$$\sum_{i=1}^4 \hat{f}_{n+1}^i = \hat{d} \int_{\hat{A}} \hat{B}^T \hat{\sigma}_{n+1} d\hat{A} = \hat{d} \int_{\hat{A}} \hat{B}^T (\Delta \hat{\sigma} + \hat{\sigma}_n) d\hat{A} \quad (24)$$

where  $\hat{\sigma}_n$  is the strain at time step  $t_n$ ,  $\Delta \hat{\sigma}$  is the incremental strain,  $\hat{d}$  is the virtual element thickness, and

$\hat{A}$  is the element area at  $t_n$ .  $\hat{\sigma}_{n+1}$  and  $\hat{\sigma}_n$  are the stress vectors at  $t_{n+1}$  and  $t_n$  respectively;  $\hat{f}_n^i$  is the nodal force, and the incremental stress is:

$$d\hat{\sigma} = \{d\hat{\sigma}_x, d\hat{\sigma}_y, d\hat{\tau}_{xy}\}^T \quad (25)$$

The nodal force at a time step of  $t_{n+1}$  is defined as

$$\hat{f}_{n+1}^i = \hat{f}_n^i + d\hat{f}^i \quad (26)$$

$$d\hat{f}^i = \{d\hat{f}_{1x}, d\hat{f}_{1y}, d\hat{f}_{2x}, d\hat{f}_{2y}, d\hat{f}_{3x}, d\hat{f}_{3y}, d\hat{f}_{4x}, d\hat{f}_{4y}\}^T \quad (27)$$

The local geometry matrix is:

$$\hat{B} = \frac{1}{J} \{B_1, B_2, B_3, B_4\}_{3 \times 8} \quad (28)$$

where  $B_i$  ( $i=1, 2, 3, 4$ ) is defined in Eqs. (14) and (15); and  $\mathbf{f}_{n+1}^i$  is the global nodal force, which is translated by

$$\mathbf{f}_{n+1}^i = \Omega^T \hat{f}_{n+1}^i \quad (29)$$

Finally, the nodal force shown in Eq. (30) can be balanced by the equilibrium equation of Eq. (1).

$$P_{\text{int},n+1}^e = \sum_{i=1}^4 \mathbf{f}_{n+1}^i \quad (30)$$

where  $P_{\text{int},n+1}^e$  is the total internal nodal force at a time step of  $t_{n+1}$ .

## 3. Material models

### 3.1 Stress-strain relationship for concrete

#### (1) Equivalent biaxial incremental model

In this research, the Darwin-Pecknold (1977) increment model was adopted as the constitutive model to calculate the structural behavior of the RC shear walls. In this model, two directions of strain and stress are considered, and are equivalent to a uniaxial model. The shear walls were supposed to be subject to an in-plane lateral load, and the response can be considered as a 2D problem. The increment of the stress and strain relationship of the equivalent 2D concrete can be represented as

$$\begin{Bmatrix} d\sigma_1 \\ d\sigma_2 \\ d\sigma_3 \end{Bmatrix} = D \begin{Bmatrix} d\varepsilon_1 \\ d\varepsilon_2 \\ d\gamma_{12} \end{Bmatrix} \quad (31a)$$

$$D = \frac{1}{1-\nu^2} \begin{bmatrix} E_1 & \nu\sqrt{E_1 E_2} & 0 \\ \nu\sqrt{E_1 E_2} & E_2 & 0 \\ 0 & 0 & (E_1 + E_2 - 2\nu\sqrt{E_1 E_2})/4 \end{bmatrix} \quad (31b)$$

where  $E_1$  and  $E_2$  are the tangent modulus in the two directions of the strain;  $\nu$  is the Poisson's ratio, which is defined as

$$\left\{ \begin{array}{l} \nu = 0.2, \text{ uniaxial compression or tension} \\ \nu = 0.2 + 0.6 \left( \frac{\sigma_2}{f_c} \right)^4 + 0.4 \left( \frac{\sigma_1}{f_t} \right)^4, \text{ biaxial tension} \\ \nu \leq 0.99 \end{array} \right. \quad (32)$$

where  $f_c$  and  $f_t$  are the uniaxial compressive strength and tensile strength of concrete, respectively.

According to Darwin and Pecknold's equivalent uniaxial strain model, the stress-strain relationship is assumed to be elastic within the increment of each load step, as shown in Eq. (33):

$$\left. \begin{array}{l} d\varepsilon_1 = \frac{d\sigma_1}{E_1} - \frac{\nu d\sigma_2}{E_2} \\ d\varepsilon_2 = \frac{d\sigma_2}{E_2} - \frac{\nu d\sigma_1}{E_1} \end{array} \right\} \quad (33)$$

The equivalent increment of the uniaxial strain  $d\varepsilon_{iu}$  is:

$$d\varepsilon_{iu} = \frac{d\varepsilon_i}{1 - \alpha \nu} = \frac{d\sigma_i}{E_i} \quad (34)$$

where  $\alpha = \sigma_1/\sigma_2$  and  $n = E_2/E_1$ ;  $\varepsilon_{iu}$  can be accumulated in the process of the loading step-by-step, as shown below:

$$\varepsilon_{iu} = \sum \frac{d\sigma_i}{E_i} \quad (35)$$

where  $\sigma_i$  is the equivalent stress.

## (2) Failure criteria

The equivalent uniaxial stress-strain curve can be defined as the above equivalent uniaxial strain. Corresponding to the Darwin-Pecknold model (1977), Saenz's compression constitutive model was adopted for the ascending branch of the concrete compressive constitutive model:

$$\sigma_i = \frac{E_0 \varepsilon_{iu}}{1 + \left[ \frac{E_0}{E_s} - 2 \right] \frac{\varepsilon_{iu}}{\varepsilon_{ic}} + \left( \frac{\varepsilon_{iu}}{\varepsilon_{ic}} \right)^2} \quad (36)$$

where  $E_0$  is the original tangent modulus and  $E_s$  is the secant modulus of maximum compressive stress.  $\varepsilon_{ic}$  is the equivalent uniaxial strain at the maximum compressive stress. To describe the stress criteria  $\sigma_{ic}$ , the Kupfer and Gerstle (1973) model was adopted (Fig. 2) as:

$$\left. \begin{array}{l} \sigma_{2c} = \frac{1 + 3.65\alpha}{(1 + \alpha)^2} f_c \\ \sigma_{1c} = \alpha \sigma_{2c} \end{array} \right\}, \quad (0 \leq \alpha \leq 1) \quad (37)$$

$$\left. \begin{array}{l} \sigma_{2c} = \frac{1 + 3.28\alpha}{(1 + \alpha)^2} f_c \\ \sigma_{1c} = \alpha \sigma_{2c} \end{array} \right\}, \quad (-0.17 \leq \alpha \leq 0) \quad (38)$$

$$\left. \begin{array}{l} \sigma_{2c} \leq 0.65 f_c \\ \sigma_{1c} = f_t \end{array} \right\}, \quad (-\infty \leq \alpha < -0.17) \quad (39)$$

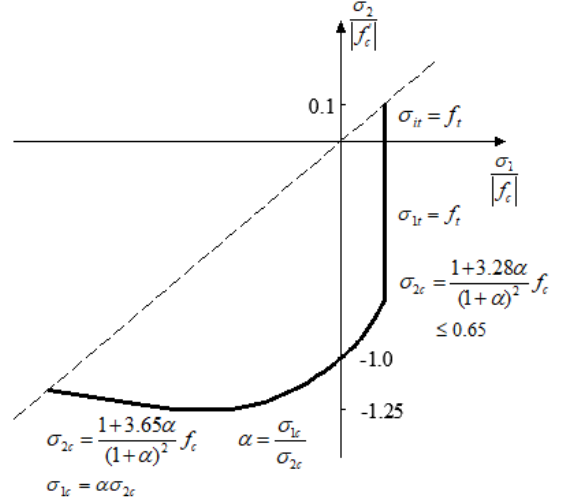


Fig. 2 Biaxial strength failure envelope of concrete (Kupfer and Gerstle 1973)

$$\left. \begin{array}{l} \sigma_{1t} = f_t \\ \sigma_{2t} = f_t \end{array} \right\}, \quad (1 < \alpha < +\infty) \quad (40)$$

where  $\sigma_{it}$  is the equivalent uniaxial tension strength of concrete in direction  $i$ ;  $\sigma_{ic}$  is the equivalent uniaxial compressive strength of concrete in the direction of  $i$  ( $i=1, 2$ );  $f_t$  and  $f_c$  are the uniaxial tensile and compressive strength, respectively.

In Eqs. (37)–(40),  $\sigma_1 \geq \sigma_2$ , and  $\varepsilon_{ic}$  can be calculated by

$$\varepsilon_{ic} = \begin{cases} \varepsilon_p \left( \frac{3\sigma_{ic}}{f_c} \right) & |\sigma_{ic}| \geq |f_c| \\ \varepsilon_p \left[ -1.6 \left( \frac{\sigma_{ic}}{f_c} \right)^3 + 2.25 \left( \frac{\sigma_{ic}}{f_c} \right)^2 + 0.35 \left( \frac{\sigma_{ic}}{f_c} \right) \right] & |\sigma_{ic}| < |f_c| \end{cases} \quad (41)$$

The compression branch of the concrete can be expressed as

$$\sigma_i = \begin{cases} \frac{E_0 \varepsilon_{iu}}{1 + \left[ \frac{E_0}{E_s} - 2 \right] \frac{\varepsilon_{iu}}{\varepsilon_{ic}} + \left( \frac{\varepsilon_{iu}}{\varepsilon_{ic}} \right)^2} & 0 < \varepsilon_{iu} \leq \varepsilon_{ic} \\ \sigma_{ic} - \frac{4}{15} E_s (\varepsilon_{iu} - \varepsilon_{ic}) & \varepsilon_{ic} \leq \varepsilon_{iu} < 4\varepsilon_{ic} \\ 0.2\sigma_{ic} & 4\varepsilon_{ic} < \varepsilon_{iu} \end{cases} \quad (42)$$

When the compressive stress of concrete  $\sigma_i$  decreases to 0.2 times of the maximum compressive strength ( $\sigma_{ic}$ ), the stress is maintained as a constant value if the strain is over  $4\varepsilon_{ic}$ . When  $\varepsilon_{iu} > 4\varepsilon_{ic}$ , the concrete is considered to be completely crushed.

The equivalent stress-strain curves of concrete subjected to tension were referred to as the bilinear model proposed by Hillerborg *et al.* (1976) as below:

$$\sigma_i = \begin{cases} E_0 \varepsilon_{iu} & 0 \leq \varepsilon_{iu} \leq \varepsilon_{it} \\ \sigma_{it} - \frac{E_0}{3} (\varepsilon_{iu} - \varepsilon_{it}) & \varepsilon_{it} < \varepsilon_{iu} < 4\varepsilon_{it} \end{cases} \quad (43)$$

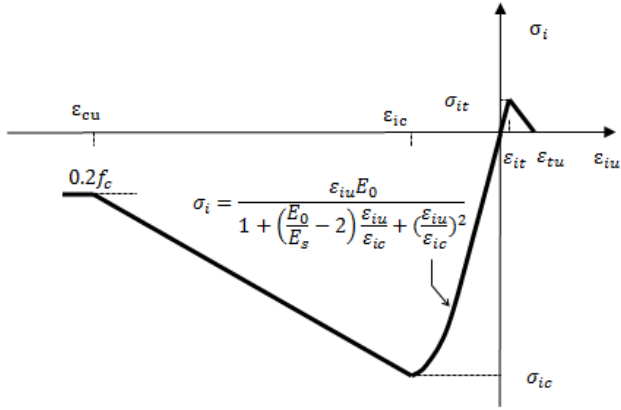


Fig. 3 Equivalent uniaxial stress-strain constitutive curve of concrete (Kupfer and Gerstle 1973)

where  $\epsilon_{it}$  and  $\sigma_{it}$  are the tensile strain and stress, according to the tensile strength, respectively.

When the material in the element reaches the equivalent ultimate tensile strength  $\epsilon_{tu}$ , cracks will appear perpendicular to the principal axis of the element. Actually, the crack tip extension, stress release, and coupling can be included in the crack development simulation. In this study, to simplify the crack behavior, a “smeared” cracking model was applied. The biaxial assumption was adopted in this model (Zhu and Dong 1985).

When a crack appears in one direction, the corresponding Young’s modulus  $E_1$  becomes zero. Cracks appear perpendicular to the primary stress of the element (shown in the diagram of Fig. 4). The stress transformation matrix is as follows:

$$D = \frac{1}{1-\nu^2} \begin{bmatrix} 0 & 0 & 0 \\ 0 & E_2 & 0 \\ 0 & 0 & E_2/4 \end{bmatrix} \quad (44)$$

In the element being analyzed, the boundary condition is satisfied even if a crack appears. When cracks appear in the element, the stress will redistribute and may cause variations of the node force. When a crack appears in both directions (as shown in Fig. 4), Young’s modulus  $E_2$  becomes zero, and the equivalent modulus matrix is:

$$D = \begin{bmatrix} 0 & 0 & 0 \\ 0 & 0 & 0 \\ 0 & 0 & 0 \end{bmatrix} \quad (45)$$

### 3.2 Constitutive model of steel bars

The bilinear model was adopted as the stress-strain constitutive relationship of the longitudinal steel bars (Fig. 5) according to the stress-strain curve of the tested steel bar (Zhang *et al.* 2014). The tested Young’s modulus value was taken as the initial Young’s modulus of steel ( $E_1$ ), and the modulus value after yielding was taken as 1% of the initial value ( $E_2$ ). The yield point of the bilinear model was

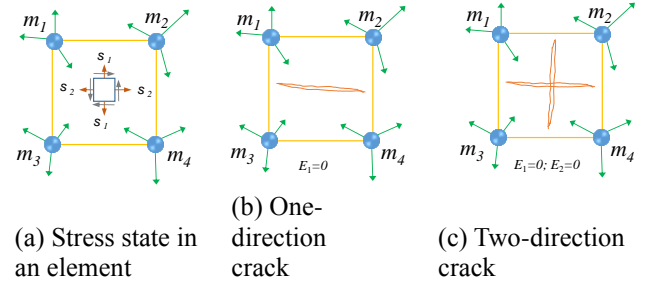


Fig. 4 Element crack diagrams

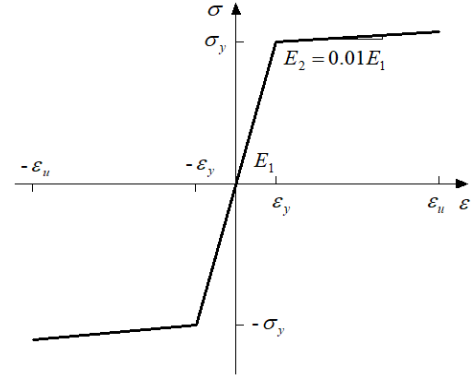


Fig. 5 Stress-strain relationship of steel bar

assigned as the yield stress and strain of the tested steel bar. The tested steel bar broke rapidly after reaching the peak strength value. Therefore, the Young’s modulus and stress were set as zero after the steel bar reached the ultimate strain. The ultimate strain was assigned as the strain at the maximum stress  $\sigma_u$ , which can be expressed as

$$\epsilon_u = \epsilon_y + (\sigma_u - \sigma_y) / E_2 \quad (46)$$

Actually, the longitudinal steel bars in the shear walls did not break even though the drift angle reached 1/120, which is the critical drift angle of collapse in the China seismic design code (GB 50011-2010, 2010). The steel bar did not reach the ultimate state in the simulation work either.

## 4. Advantages

In the continuum-based traditional finite-element theory, the global stiffness matrix needs to be calculated, e.g., using the immediate integration method and the mode superposition method (Bathe and Wilson 1976), in order to obtain the internal forces of the structural element. Therefore, the large stiffness matrix needs to be recalculated for the nonlinear displacement at each time, which requires significant computational overhead. Furthermore, the ill-condition of the stiffness matrix may cause serious errors. For large deformation problems, the equilibrium condition depends on the configuration after deformation, and the iteration is involved in solution, which makes the solving process complex (Wang and Shao, 1997). In this study, the advantages of the four-node element based on vector mechanics in the simulation of structural behavior are discussed.

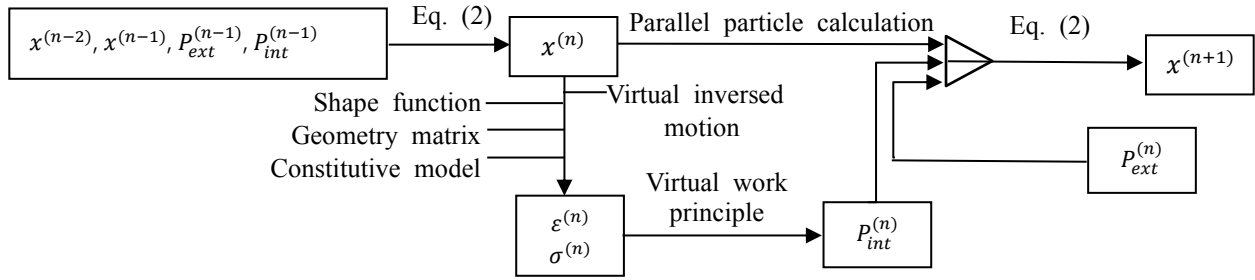


Fig. 6 Flow chart showing calculation

### (1) Independent equation of motion

The presence of independent particles is one of the important characteristics of vector mechanics. A continuous object component is decomposed into a finite number of particles. The component mass is concentrated on the particles, and the motion of the particles is balanced according to Newton's law. Each mass has its own kinematic equation, thus providing an iterative position. Compared with the large system equation of motion, it is easy to obtain the individual displacement for independent particles. The probability of ill-condition in the global stiffness matrix for nonlinear problems is substantially reduced. In this four-node element, the solution of internal forces depends on the motion of four particles. For the simulation of concrete nonlinearity, the variations in material properties and large deformation are addressed using the independent particle motion equation.

### (2) Separation of rigid body motion

The virtual inverse motion in vector mechanics is developed to obtain the pure deformation of the particles (Ting, et.al., 2012; Duan, et.al., 2017). The rigid body translation and rotation in the virtual inverse motion method can be separated from the deformation, and the internal force is obtained from the pure deformation. The conversion matrix of the rigid body motion can be used to calculate the pure deformation, after which the actual position is obtained. Compared with the traditional FEM, the stiffness matrix and internal force expression can be greatly simplified, and has a significant advantage in calculation efficiency (Ting *et al.* 2004b). The process of the calculation for the strain can also be simplified by the separated rigid body motion.

### (3) Unified analysis process

Generally, to obtain the internal force and deformation, three main concepts are used (Ting, et. al. 2012): ① particle description; ② path element (segmented motion along path); and ③ virtual inverse motion. Two main iteration cycles are concerned in the calculation. One is evaluation of the internal forces using the virtual inverse motion on the deformed element, and the other is computation of the nodal displacements using Eq. (1) (Ting, et. al. 2012; Duan, et. al., 2017). The flow chart of the main cycle of the program is shown in Fig. 6. Given the position of the two former steps, and the former external and internal forces, by applying Eq. (2), the position of the current time

step can be obtained. Combined with the virtual inverse motion, the element stress and strain can be computed. The internal force can also be derived by applying the virtual work principle. Using the newly obtained information, the next cycle can be started.

Vector mechanics provides a unified analysis framework that is concise and systematic. The spatial variation and geometrical transformation can be processed efficiently by the particle description, virtual inverse motion, and path element (Ting *et al.*, 2004a) in order to reach the solution of the whole deformation and damage. Actually, the particle description and path element enable the continuous deformation and characteristic changing of the simulated object to conduct the corresponding simulation. The calculation process is not limited by geometric nonlinearities, even though there is a discontinuous behavior. Cracking, crushing, and collapse always induce instability or in-convergence of calculations for general continuum-based finite-element theory. For this reason, the spatial motion, geometric transform, and material character changing of the individual element or integral structure can be processed in this generalized framework.

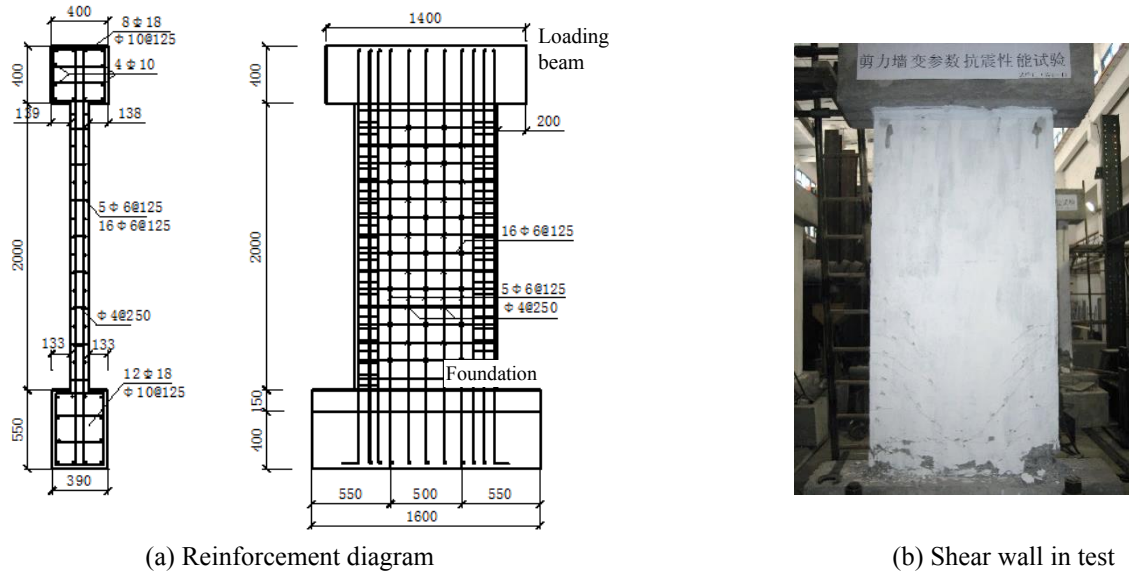
In this paper, the plane element deformation problem of shear walls is simulated by the developed vector mechanics-based four-node planar element, which takes the advantage of the VFIFE method.

## 5. Simulation verification

### 5.1 Experiment for comparison

A group of experiments on RC shear walls with dimensions of 2000 mm × 1000 mm × 125 mm was performed to verify the effectiveness of the four-node planar element for a static problem. The experiments were conducted in the National State Key Laboratory of Civil Engineering at the Tongji University (Zhang *et al.* 2007), as shown in Fig. 7. Embedded columns were designed according to the Chinese Seismic Design Code (GB 50011-2010).

Four shear wall specimens with different vertical loads or concrete strengths tested under a low-cyclical load were simulated. The vertical load and the horizontal load were exerted by a hydraulic jack on the top beam, and the actuator was controlled by the displacement. The compressive strengths of the concrete were determined to be 30.8 MPa and 20.7 MPa. The diagram of the shear wall SW-A, which is similar to that of other specimens, is shown



(a) Reinforcement diagram

(b) Shear wall in test

Fig. 7 Reinforcement and dimensions of shear wall SW-A (unit: mm)

Note: Steel type of HPB is listed as “ $\phi$ ,” and HRB as “ $\Phi$ .”

Table 1 Parameters and loading of experimental shear walls

Label of specimen	Size of specimen (mm)	Aspect ratio	Compressive strength of concrete (MPa)	Length of constraint area (mm)	Vertical load (kN)	Boundary longitudinal reinforcement	Stirrup
SW-A	2000 × 1000 × 125	2	20.7	200	246	6 $\Phi$ 10	$\phi$ 6@80
SW-B	2000 × 1000 × 125	2	20.7	200	493	6 $\Phi$ 10	$\phi$ 6@80
SW-C	2000 × 1000 × 125	2	20.7	200	739	6 $\Phi$ 10	$\phi$ 6@80
SW-D	2000 × 1000 × 125	2	30.8	200	1380	6 $\Phi$ 10	$\phi$ 6@80

in detail in Fig. 7. The specimen parameters and loading scheme are listed in Table 1.

## 5.2 Modeling of the RC shear walls

### 5.2.1 Model construction

The shear walls were modeled according to the test specimens, as shown in Fig. 8 using the planar element. The mass of the shear wall is assigned to the nodes (Ting *et al.*, 2004a). Each rectangle is modeled using the four-node planar element, which is connected to the surrounding elements, and satisfies the deformation coordination condition. The number of elements varies with the size of specimens, which impacts the effectiveness of the simulation results. The shear wall was divided into boundary columns and core walls according to the different restraining conditions. In this study, the concrete member was modeled by four-node planar element, and the reinforcement was described using a two-node fiber element. As shown in Fig. 8, there are 198 nodes, 170 four-node planar elements, and 367 fiber elements in the RC shear wall model. The bottom of the model were completely restrained, corresponding to experimental boundary conditions. The sliding and buckling effects were not considered because those were not clearly observed during the tests.

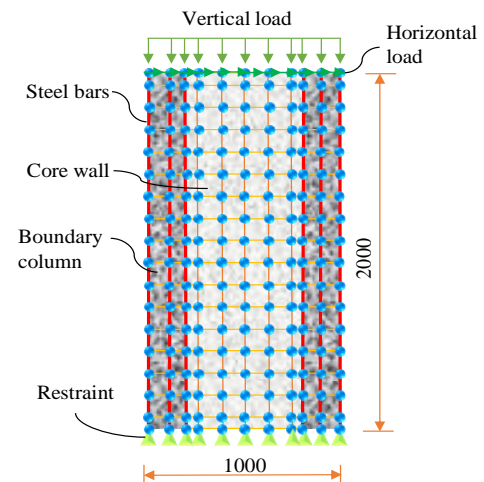


Fig. 8 Simulation model (unit: mm)

### 5.2.2 Material properties

The properties of concrete and steel bars were assigned according to the experimental results and are listed in Tables 2 and 3. In the constitutive model, introduced in Section 3, the strength and ultimate strain of the confined concrete within the boundary column (as shown in Fig. 8)

Table 2 Properties of the boundary longitudinal steel bars

Steel type	Φ10
Area (mm <sup>2</sup> )	63.62
Yield strength (MPa)	379.00
Ultimate strength (MPa)	554.00
Modulus of Elasticity $E_1$ (10 <sup>5</sup> N/mm <sup>2</sup> )	1.812
Yield strain	0.002092
Post-yield stiffness $E_2$	0.01 $E_1$

were assigned as 1.1 times those of the unconfined concrete (Zhang, 2007); thereby, the concrete constraint effect was considered.

The concrete and steel bar share the same nodes at the crossing points. Concrete cracking and crushing were considered using the reduced Young's modulus, and the steel bars were simulated as a bilinear model until they attained the ultimate state, as described in Section 3. The concrete and steel bar density were set to  $2.5 \times 10^4$  kN/m<sup>3</sup> and  $7.8 \times 10^4$  kN/m<sup>3</sup>, respectively.

### 5.2.3 Loading sequences

The large deformation process was simulated subject to a pushover load in order to test the stability and accuracy of the developed model. Previous studies reported that the force-displacement curves of RC shear walls subjected to a pushover load are close to the skeleton curve from a low-reversed cyclical experiment (Dong and Lu 2007). The error between monotonic loading specimens with cyclical loading specimen is within 1.5% before reaching the peak strength value, and after that, the error is within 2.5% (Dong and Lu 2007). The experiments conducted by Zhang *et al.* (2019) and Lefas *et al.* (1990) also demonstrate similar results that simplify and show the adaptability of the equation of motion in the vector mechanics for a static problem. The simulated lateral load-displacement was then compared with those of the static cyclical experiment.

The top beam was set as a rigid body, and the bottom foundation was described as a fixed restraint. In the simulations, the vertical and horizontal loads were added to the top beam of the specimens uniformly. Two loading sequences were examined; they involved the vertical and horizontal displacement loading. The vertical loads are listed in Table 1 and were increased gradually in 10 s, which remained until the final simulation. After an interval of 5 s to eliminate the dynamic response, the horizontal displacement load was applied gradually over the next 100 s until the top horizontal displacement reached 30 mm (Fig. 9). In total, the entire loading sequence lasted 120 s. The time step for the analysis was set as  $10^{-4}$  s<sup>-1</sup>, and the results were recorded every 0.1 s. The damping coefficient of the shear walls was set to a large value ( $1.0 \times 10^4$  s<sup>-1</sup>) to eliminate the damping effect, in order to reach a static loading effect.

### 5.3 Computational resources

The four-node planar element and the corresponding program were compiled using the Intel Visual Fortran 15.0

Table 3 Properties of the concrete of the simulated model

Label of specimen	Compressive strength (MPa)	Compressive strength of confined concrete (MPa)	Ultimate compressive strain	Ultimate compressive strain of confined concrete
SW-A	20.7	22.7		
SW-B	20.7	22.7	0.0033	0.00363
SW-C	20.7	22.7		
SW-D	30.8	33.9		

Table 4 Laptop configuration

Items	Description
Host	LENNOVO 81BS
Cache	8 MB
Memory	8 GB
CPU Clock Speed	1.80 GHz
CPU	Core i7-8550U
Hard Disk Drive	Solid-state disk (256 GB)

compiler. The model was run on a laptop whose computer configuration is described in Table 4. The calculation time for modeling the RC model described above was 7620 s. Meanwhile, the required computational resources are: CPU utilization: 11.0%—21.3%; Memory usage: 6.2 MB; Data storage: 339 MB for 1,200,000 analysis steps.

From Fig. 9, it can be observed that the simulated deformation of the RC shear walls under the above conditions behaves as expected, even when the drift angle is over 1/120, which is the collapse criteria specified by the seismic design code (GB50011-2011).

## 5.4 Simulation results and verification

### 5.4.1 Plan for static analysis

As mentioned above, the equation of motion was adopted to determine the dynamic behavior of a structure in vector mechanics. However, to eliminate the dynamic impact in static problems, a simplified approach is to load using a slow and uniform speed, and to assign an extremely large damping ratio. Thus, the structural responses will eventually converge to a stable value, which is considered as the actual static solution.

Based on this concept, the static solution is obtained, which disregards energy dissipation. This simplified method is achieved by adding a virtual damping force to each motion equation (Eq. (1)), resulting in:

$$f_d = \begin{bmatrix} f_{du} \\ f_{dv} \end{bmatrix} = -\xi m \frac{d}{dt} \begin{bmatrix} u \\ v \end{bmatrix} \quad (47)$$

There are two factors that impact the computed results in Eq. (47), including the damping factor  $\xi$  and  $\dot{x}$ . The damping factor  $\xi$  does not represent a real damping, but a virtual damping for the calculation of the responses of static loading. A relatively large damping factor can eliminate the

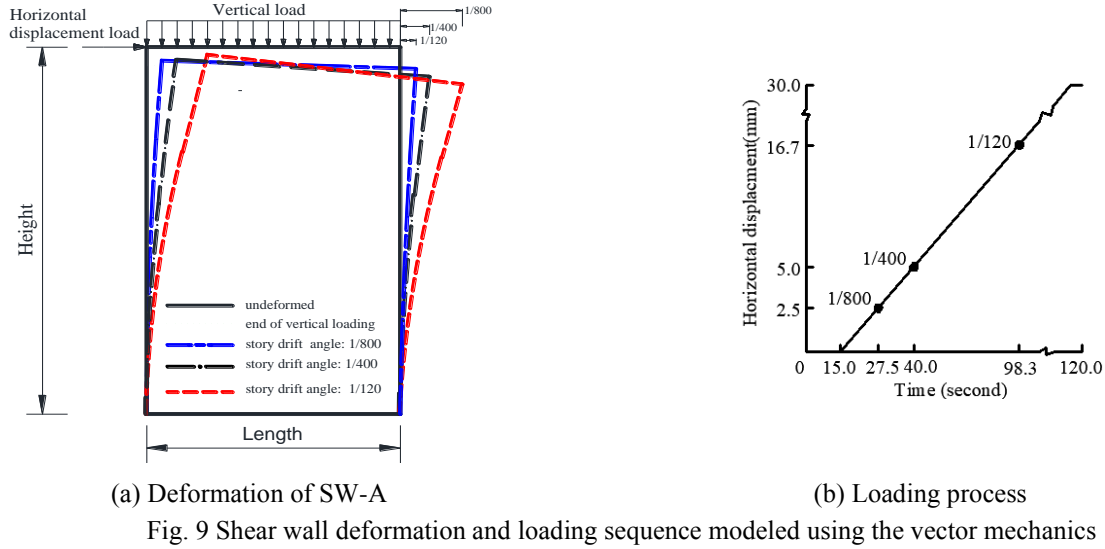


Fig. 9 Shear wall deformation and loading sequence modeled using the vector mechanics

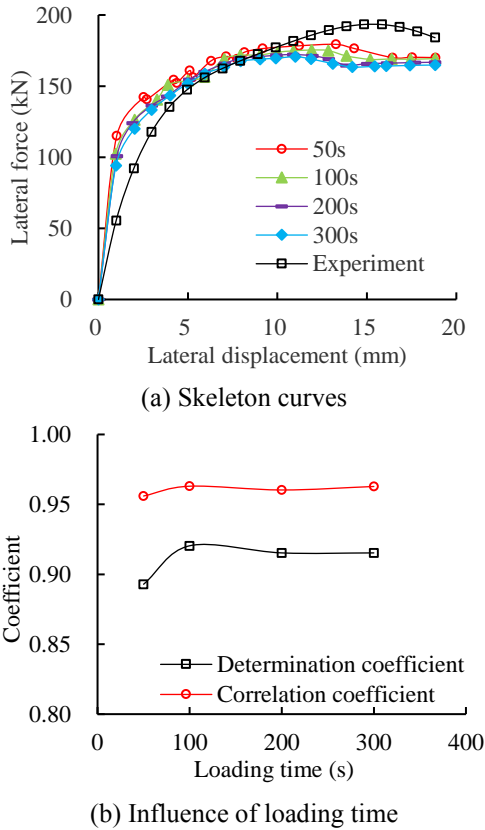


Fig. 10 Loading time analysis

vibration, and  $\dot{x}$  is required to be extremely small in order to eliminate the damping force. Therefore, the loading time is designed to be long according to a specific requirement. The integral time step can be a small value in order to realize that process.

#### 5.4.2 Loadings for simulation analysis

Taking SW-A as an example, the deformation and the lateral loading process are shown in Fig. 9 (a) and (b). As described in Section 5.2.3, the vertical load was first applied, followed by the increasing lateral load. The

position of a particle during the loading process is represented by the deformation diagram of the RC shear wall (Fig. 9a). Under the vertical load, the specimen was first compressed; as the lateral load increased, the specimen then gradually bent to one side. The lateral deformation increased until the loading procedure stopped when the specimen was experimentally failed. The drift angles when the specimens failed are observed over the limitation of 1/120, which is specified as critical collapse criticize of Chinese seismic code.

#### 5.4.3 Discussion on simulation parameters

As shown in Figs. 10-12, the simulated behavior agrees fairly well with experimental observations. The effect of the simulation parameters on damping factors and loading speed were evaluated based on this simulation model. In addition, the meshing quality is a critical factor that may impact the simulated response results of the finite-element analysis. Accordingly, simulations were then performed on the loading speed, damping factor, and mesh quality of elements.

##### (1) Loading speed

Four kinds of loading time span were examined: 50 s, 100 s, 200 s, and 300 s, corresponding to different loading speeds. The lateral load was controlled by the lateral drift angle (lateral displacement relative to the story height), and the target lateral drift angle was set to about 1/100 according to the experimental tests.

Fig. 10(a) shows the lateral force-top lateral displacement curves simulated for four different loading specimens along with of the tested specimens. The influence of the loading time on the determination coefficient  $R^2$  [ $R^2 = 1 - SSE$  (sum of squares error)/ $SST$  (sum of squares in total)] and correlation coefficient ( $r$ ) is shown in Fig. 10(b). It can be observed that the simulated results are enhanced when the loading time was long (loading speed was slow). Both these coefficients,  $R^2$  and  $r$ , for the loading time of 100 s were higher than those for a loading time of 50 s, and they remained relatively stable. In other words, the simulation results converged to a static solution

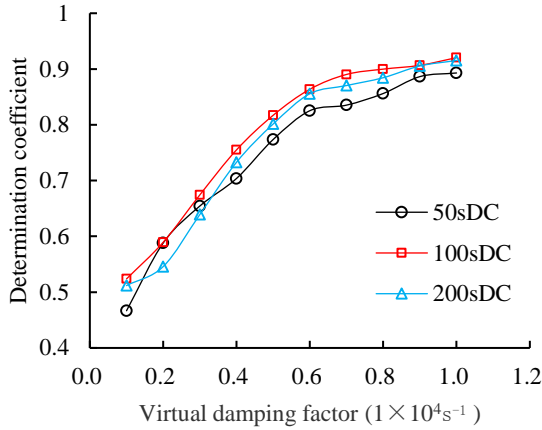


Fig. 11 Influence of the virtual damping factor

when the loading time exceeded 100 s. Accordingly, the loading time of 100 s was adopted for subsequent analyses.

### (2) Virtual damping factor

Different virtual damping factors were evaluated to find a value that kept the simulation system stable, and converged to the static solution. With reference to the example (Ting, 2012), the initial damping factor was set to  $1.0 \times 10^4 \text{ s}^{-1}$ , which represents in  $C_1$  and  $C_2$  in Eq. (2) as 1.333 and 0.333, respectively. Then, the damping factor values that were analyzed ranged from  $0.1$ – $1.0 \times 10^4 \text{ s}^{-1}$  with increments of  $0.1 \times 10^4 \text{ s}^{-1}$ . Each increment was tested under three lateral loading speeds (i.e., lateral loading times of 50 s, 100 s, and 200 s after vertical loading).

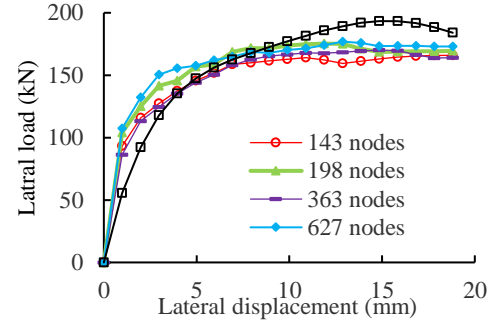
The determination coefficient and virtual damping factor relationship are presented in Fig. 11. As shown in the figure, the error ( $\sqrt{1 - R^2}$ ) in simulation is enhanced when the virtual damping factor increases, after which the improvement becomes gradual and maintains a constant value at about 0.9 when the damping factor exceeds  $1.0 \times 10^4 \text{ s}^{-1}$ . Fig. 11 also indicates that the loading speed does not significantly influence the determination coefficient ( $R$ ) when it exceeds 100 s. Consequently, the virtual damping factor was set to  $1.0 \times 10^4 \text{ s}^{-1}$  in subsequent analyses.

### (3) Meshing quality

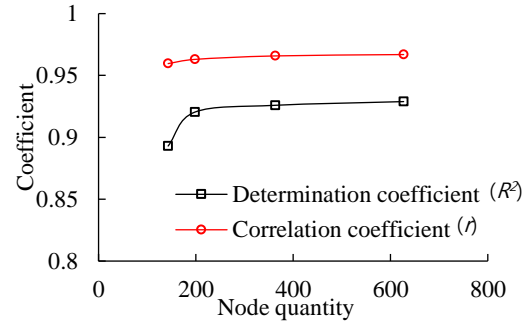
The simulation accuracy generally depends on the meshing quality in FEMA, which was also analyzed in this study. Four types of meshing quality were used, resulting in 143, 198, 363, and 627 nodes, which were subject to a loading speed of 100 s and a virtual damping factor of  $1.0 \times 10^4 \text{ s}^{-1}$ . Fig. 12(a) shows the lateral force-top horizontal displacement skeleton curves of the calculation results. Fig. 12(b) shows the determination coefficient and correlation coefficient. Fig. 12 indicates that the correlation coefficient of the fine meshed specimen (with larger number of nodes) is higher than those with lower nodes when compared with the experimental results. Meanwhile, the increase is not as obvious as when the number of nodes exceeds 198, as shown in Fig. 12(b). Since the computation time substantially increases with meshing quality, a mesh with 198 nodes was used for subsequent analysis.

Table 5 Error analysis of the skeleton curves

Label of specimen	Coefficient of determination	Correlation coefficient
SW-A	0.9204	0.9630
SW-B	0.9337	0.9751
SW-C	0.8393	0.9569
SW-D	0.9530	0.9829



(a) Skeleton curves



(b) Correlations

Fig. 12 Influence of node quantity on the load-displacement relationship

## 6. Simulation results and discussion

As discussed above, the loading speed of 100 s, damping factor of  $1.0 \times 10^4 \text{ s}^{-1}$ , and a mesh with 198 nodes were adopted in the static push-over analysis for the RC shear walls with different design or loading conditions (Zhang *et al.* 2007). The lateral force-displacement behavior was analyzed from the initial state of zero-deformation and zero-speed, and it was then terminated after it was near collapse according to the experiment results. The vertical load was added to the top beam, which is the same as the process introduced in Section 5. Then, the lateral load was added uniformly at the top beam after 100 s.

### 6.1 Lateral force-displacement curves

The lateral force-top displacement curves of the four RC shear walls, including the simulated results (marked as Planar E.) and the experimental results (Experiment), are shown in Figs. 13(a)–13(d). The errors of the simulated results for each specimen compared with the experimental results are listed in Table 5. It can be observed that the coefficients of determination of the four specimens (SW-A, SW-B, SW-C, and SW-D) were 0.9204, 0.9337, 0.8393,

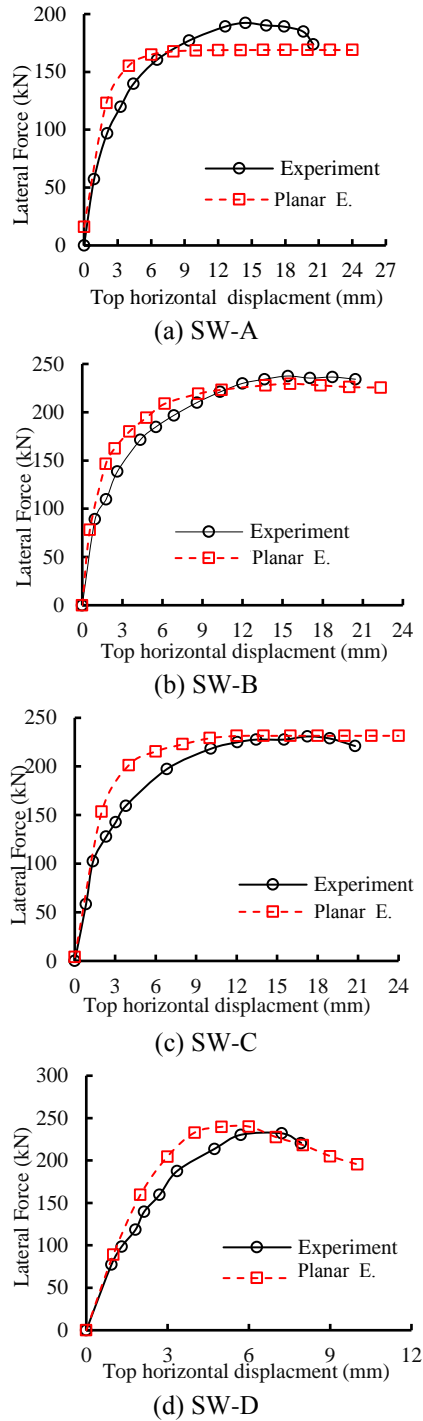


Fig. 13 Skeleton curves of the shear walls

and 0.9530, respectively, and the correlation coefficients ranged from 0.9569 to 0.9829, which indicates that the lateral force-top horizontal displacement curves simulated by the four-node planar elements correlated well with the experimental observations. The lateral load-displacement curves in Fig. (13) also demonstrated that the initial stiffness values of the simulated results are larger than those of the experiment results although the peak lateral force is almost the same. The larger initial stiffness in this analysis is considered to be related to the idealized assumptions, i.e., no steel sliding and no defect in the cast.

Table 6 Error analysis of the simulated maximum moment-curvature relationship

Label of specimen	Coefficient of determination $R^2$	Correlation coefficient $r$
SW-A	0.8946	0.9534
SW-B	0.9421	0.9903
SW-C	0.7526	0.8990
SW-D	0.9637	0.9986

## 6.2 Curvature development along height

For shear walls, the bending resistance capacity is an important index of seismic performance. With the traditional FEM, it is difficult to simulate the large flexural behavior owing to the assumption of a small deformation when evaluating the curvature development. The curvature development was analyzed and compared with the experimental results in this study. Figs. 14–17 show the curvature distributions along the height of the four shear walls subject to different drift levels. The inter-story drift angles of 1/1000, 1/800, 1/400, and 1/120 were selected (specimen SW-D did not reach 1/120, but reached the ultimate state at a drift angle of 1/250). These four drift angles were considered as the deformation limitations of seismic resistance levels corresponding to the performance states of “Immediate Occupancy,” “Repair,” “Life Safety,” and “Collapse,” respectively (Thomsen, et.al., 2004). The curvature was obtained from the strain gages along the steel bars on both sides of the shear walls, and was basically linearly distributed before the drift angle reached 1/400, after which the curvature at the lower part of the wall increased rapidly. This rapid increase generally causes the unstable computation or non-convergence for the traditional finite-element approach.

Figs. 14–17 show that the correlation coefficients ( $r$ ) exceed 0.9 in all cases, and the coefficients of determination ( $R^2$ ) are also fairly close to 1.0, even at the stage of large deflection. This demonstrates the accuracy of the simulation results on the curvature development, even in the stage with the rapidly increase.

## 6.3 Maximum curvature vs. moment

Generally, the maximum curvature of the bottom section development shows the failure development of the bending element. The maximum moment-curvature curves of the four RC shear walls at the bottom are shown in Figs. 18(a)–(d). Table 6 shows the degrees to which the simulated maximum moment-curvature relationship agreed with the experimental observations.

As observed in Fig. 18, the simulated maximum moment-curvature relationship closely matched the experimental observations. Data in Table 6 show that the coefficients of determination are 0.8946, 0.9421, 0.7526, and 0.9637 for walls SW-A, SW-B, SW-C, and SW-D, respectively. Owing to the limitation of the experimental data, the error of SW-C is slightly higher than that for other specimens. The errors are considered to be caused by specimen construction and the testing system. Basically, the simulated and tested maximum moment-curves are very similar.

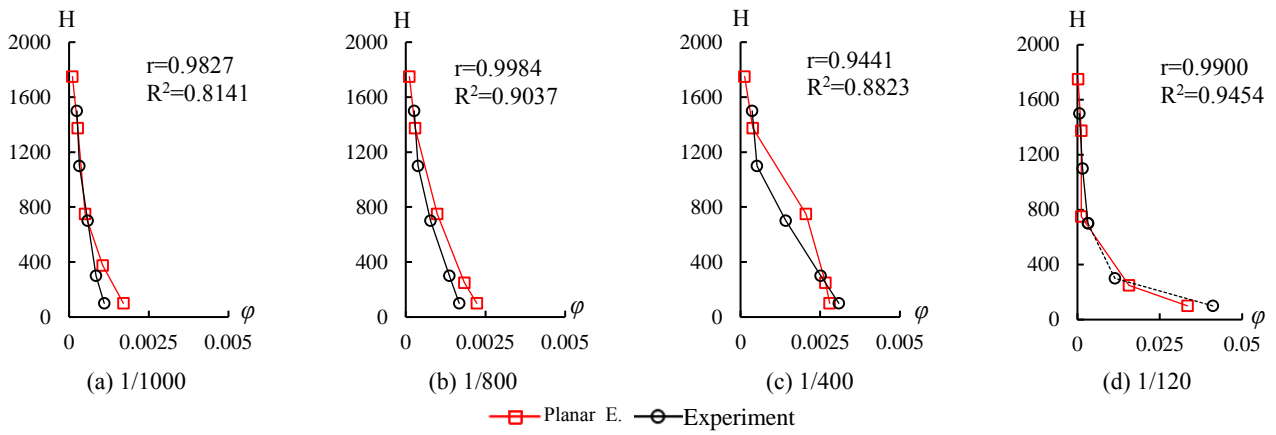


Fig. 14 Curvature along height for different drift angle: SW-A

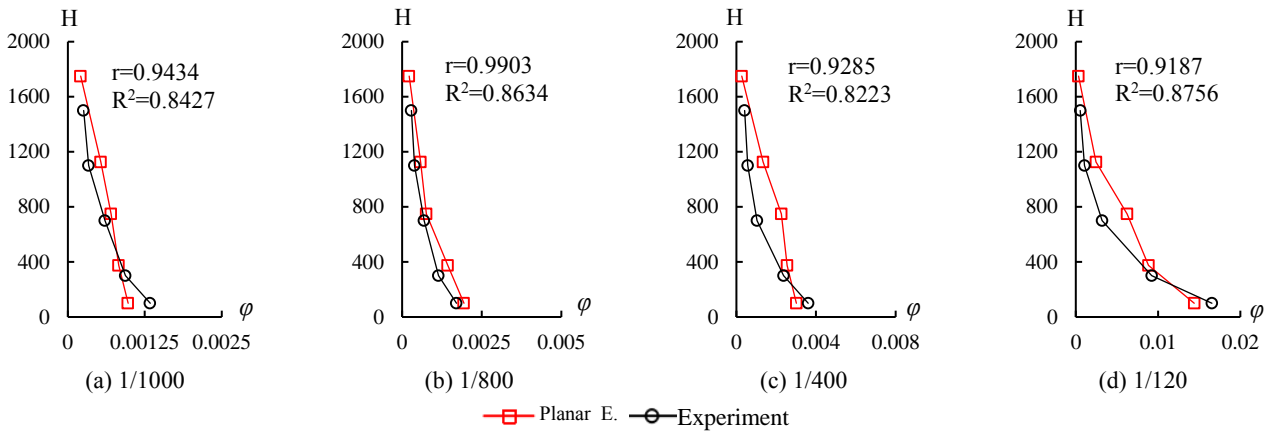


Fig. 15 Curvature along the height for different drift angles: SW-B

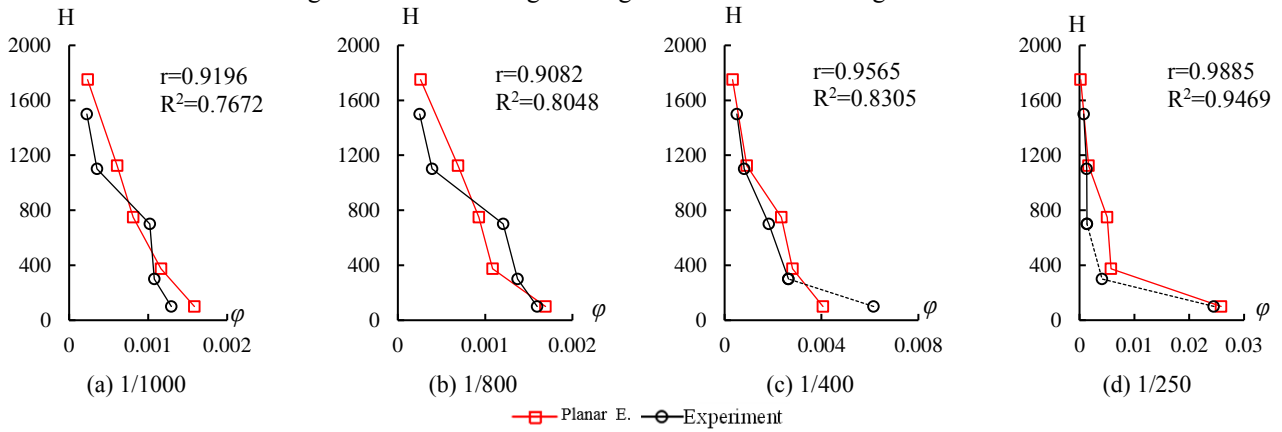


Fig. 16 Curvature along the height for different drift angles: SW-C

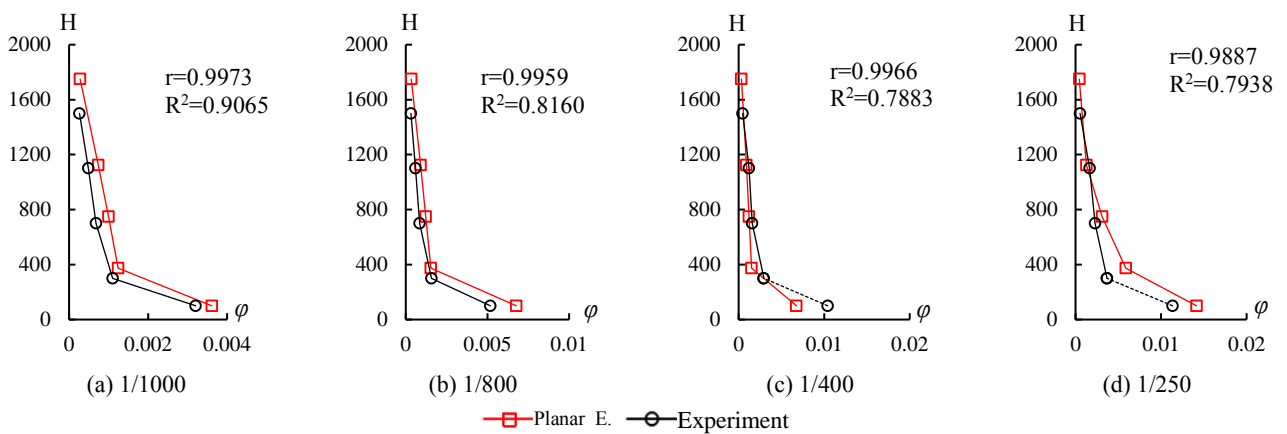


Fig. 17 Curvature along the height for different drift angles: SW-D

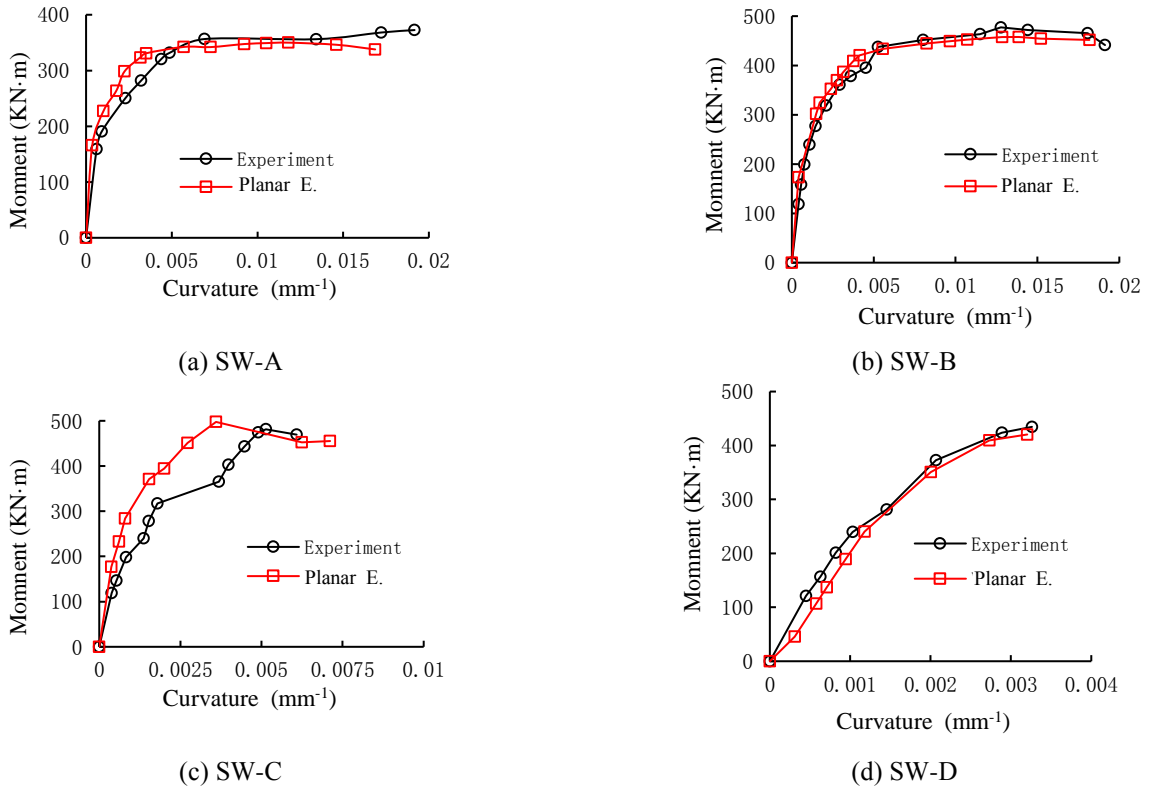


Fig. 18 Maximum moment-curvature curves at the bottom

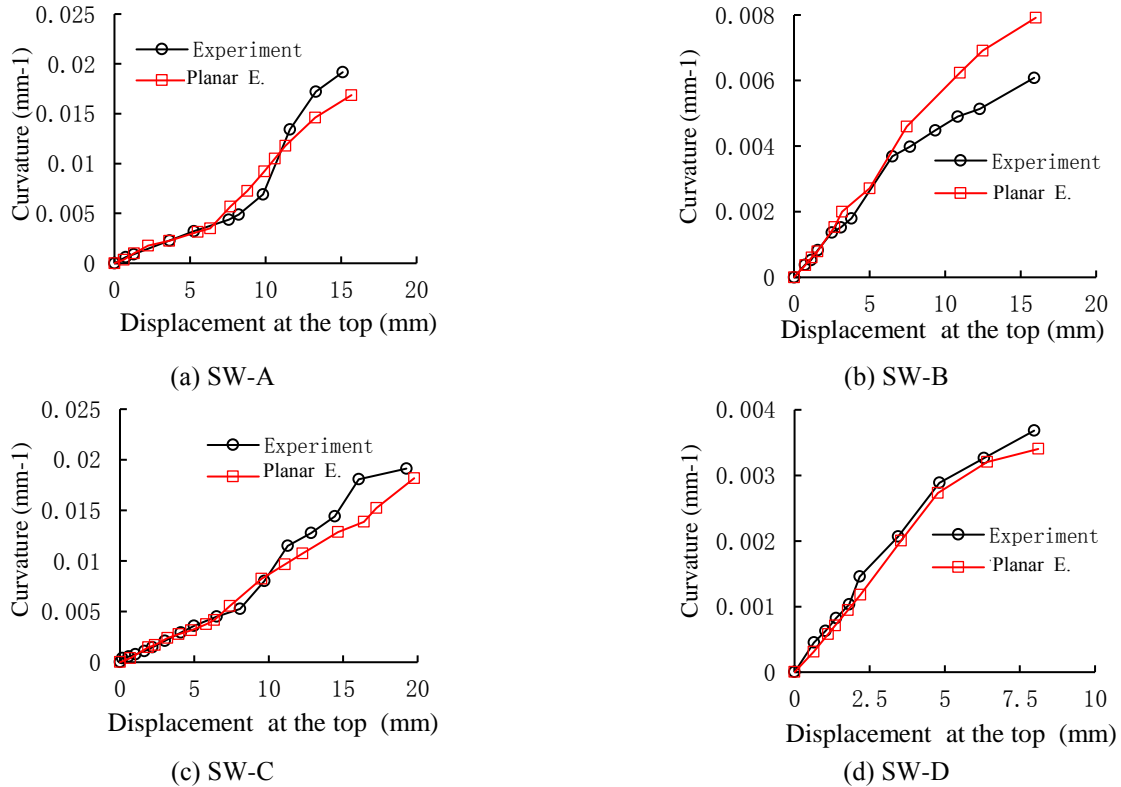


Fig. 19 Maximum curvature-displacement curves

#### 6.4 Maximum curvature vs. top displacement

The maximum curvatures developed as the displacement increased are analyzed and shown in Figs. 19(a)-(d). The

maximum curvature was obtained from the strain gages on the outside steel bars at the bottom section of the shear walls. In these experiments, for the specimens with a flexure domain pattern, the maximum curvature occurred at

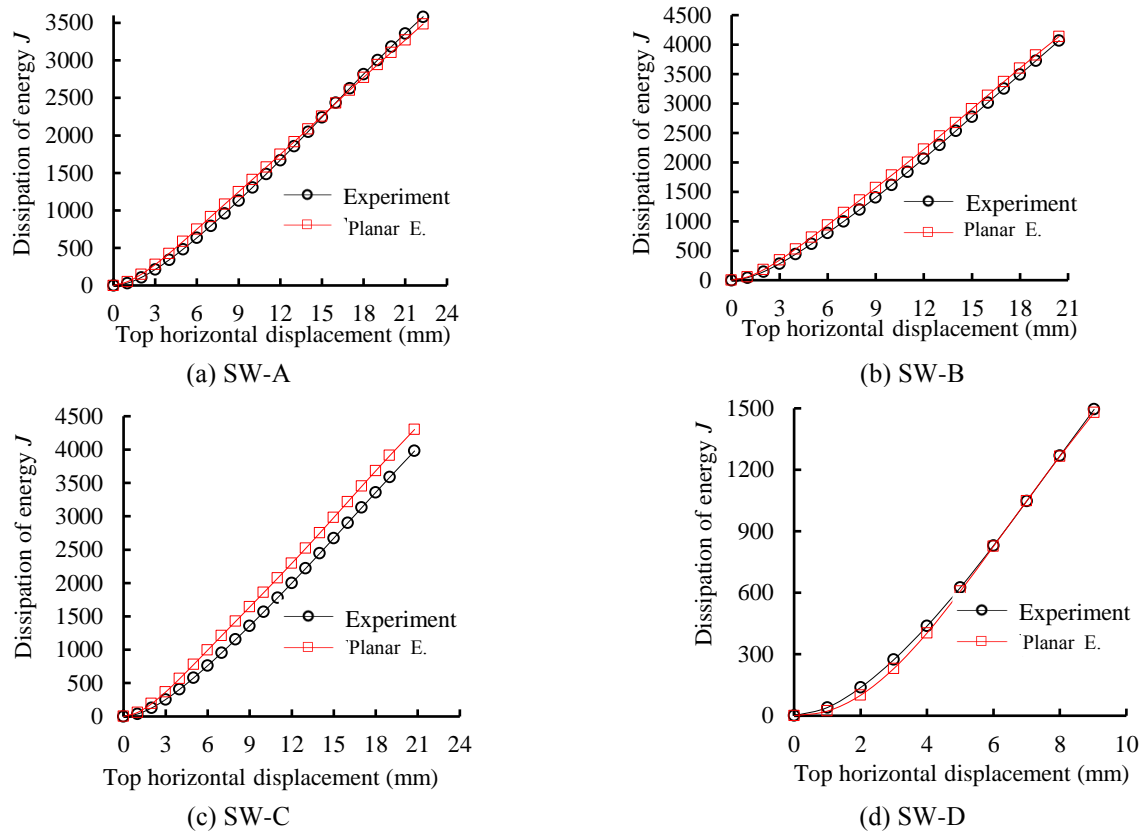


Fig. 20 Dissipation of energy

Table 7 Error analysis of the simulated maximum curvature–displacement relationship

Label of specimen	Coefficient of determination $R^2$	Correlation coefficient $r$
SW-A	0.9661	0.9832
SW-B	0.9255	0.9892
SW-C	0.8926	0.9751
SW-D	0.9832	0.9986

the bottom section of the walls, which was similar to the results presented in Section 6.2. The displacement shown in Fig. 19 was the lateral displacement at the top of the shear wall when the bottom section of the wall reached the maximum curvature. Table 7 shows the error analysis of the simulation efficiency.

Fig. 19 and Table 7 also demonstrate the close results of the maximum curvature development to the tested results.

### 6.5 Energy dissipation

Figs. 20(a)–(d) show the simulated and tested energy dissipation -top displacement curves of the four shear

walls. The energy dissipation is obtained from the integral of the lateral force-top displacement curves. Both the simulated and tested energy dissipation values increase as the lateral displacement increases. The growth gradient is first gradual, and then increases rapidly and then tends to be relatively constant. For comparison, Table 8 shows the comparison results between simulations and experiments.

Fig. 20 and Table 8 show that the coefficients of determination are 0.9953, 0.9909, 0.9559, and 0.9979 for walls SW-A, SW-B, SW-C, and SW-D, respectively. The correlation coefficients are all above 0.99. The error of the total dissipation of energy ((simulated results-tested results)/ tested results) are all smaller than 10%, which indicates that the simulation results of the planar element model agrees well with the experimental data.

### 6.6 Crack distribution

Besides the deformation performance, concrete damage, including cracking and crushing are also important in the evaluation of seismic performance. In this study, concrete cracks are assumed to be uniformly distributed in the

Table 8 Error analysis of the simulated dissipation of energy-top horizontal displacement curves

Label	Coefficient of determination $R^2$	Correlation coefficient $r$	Total dissipation of energy - experiment $J$	Total dissipation of energy - planar element on VM $J$	Error
SW-A	0.9953	0.9990	3582.73	3485.42	2.72%
SW-B	0.9909	0.9994	4068.81	4139.48	1.74%
SW-C	0.9559	0.9991	3978.80	4301.39	8.11%
SW-D	0.9979	0.9996	1494.68	1478.67	-1.07%

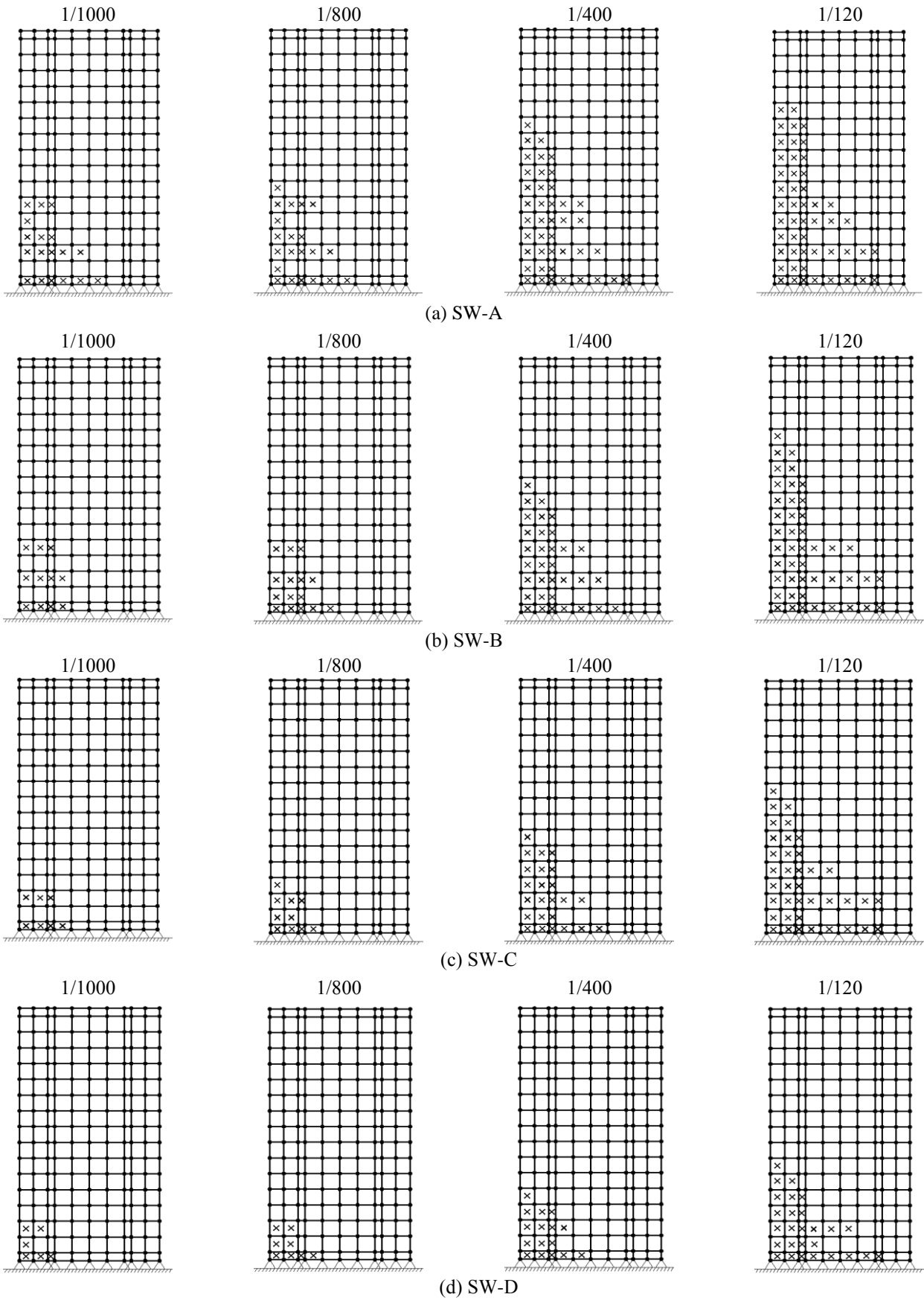


Fig. 21 Simulated crack distribution for various drift angles in shear walls

element when the tensile strain exceeded the critical value ( $4\varepsilon_{it}$ ) in the simulation of the RC shear walls. Then, the planar element was considered to be cracked from that time. Similarly, concrete crushing occurred when the compressive strain exceeded  $4\varepsilon_{ic}$ ; thereafter, the concrete stress maintained a constant value of  $0.2\sigma_{ic}$  when the element was compressed. Although the mentioned cracking and crushing constitutive model are simplified, it can also provide a solution to solve the simulation and evaluation for this kind of damage problem.

Figs. 21(a)–(d) show that when the lateral drift angle varies from 1/1000 to 1/120, the distribution of cracks increased and gradually extended to the upper and inner parts of the shear walls. Figs. 21(a)–(c) show that the crack distribution decreased as the axial ratio (ratio of vertical load to the section strength) increased, which is in accordance with experimental findings (Zhang 2007).

Figs. 21(c)–(d) show that when the shear walls had the same axial ratio but different values of concrete strength, fewer cracks developed in the shear wall with higher concrete strength. In addition, there were fewer cracks in the elements near to the already-cracked element, which was attributed to local stress release. The concrete cracking and crushing simulation also provides evidence of the influence of the axial ratio and concrete strength. The crack development results obtained from the developed program indicate that the damage simulation of concrete cracking and crushing was in good agreement with the actual behavior of experimental shear walls. The strain distribution and development simulated by the planar element accurately shows the damage evolution. Furthermore, the analysis of fracture behavior, such as concrete cracking and crushing, steel bar buckling, and even the collapse of a structural member can be carried out by the four-node planar element model simulation platform, with a corresponding constitutive model and refined time step. However, the accurate simulation on the cracking mechanics are still deserved further verification considering cracking pattern, cracking mode, and interaction of concrete and steel bars.

## 7. Conclusions

In this paper, the concrete damage involving a large deformation of RC shear walls was effectively simulated by the vector mechanics using the four-node planar element framework. The simulated responses are found to be in good agreement with experimental results. In summary, the following conclusions are made:

- (1) The large deformation behavior is successfully solved by the developed four-node element based on vector mechanics using as well as the corresponding composed biaxial material constitutive model and damage model;
- (2) The static response can be obtained by solving the equation of motion in this vector mechanics-based procedure. Low speed, large damping factor, and a reasonable meshing scheme can be found to have stable and acceptable static response results;
- (3) Concrete cracking and crushing in the ultimate stage are also expected to achieve close simulation results to the

experiment results using the simplified damage behavior simulations.

This study provides a framework to analyze the entire damage process of concrete structures, including large deformation, material nonlinearity, and predictions of the structural behavior when suffering from property degradation and sudden disaster. Future works will investigate the seismic behavior evaluation for common 3D elements or structures, the development of multiple kinds of material constitutive modules, including damage criteria, concrete cracking or crushing, and the interaction between reinforcement and concrete.

## Acknowledgments

The authors gratefully acknowledge the financial support provided by the National Natural Science Foundation of China (51578419, U1709216 and 51522811) and the National Key R&D Program of China (2018YFE0125400, 2017YFC0806100).

## References

- Amir, Ayoub, and Filippou C.F. (1998), “Nonlinear finite-element analysis of RC shear panels and walls”, *J. Struct. Eng.*, **124**(3), 298-308. [https://doi.org/10.1061/\(ASCE\)0733-9445\(1998\)124:3\(298\)](https://doi.org/10.1061/(ASCE)0733-9445(1998)124:3(298)).
- Bathe, K.J. and Wilson, E.L. (1976), *Numerical methods in finite element analysis*, Prentice Hall, Englewood Cliffs, NJ, USA.
- Darwin, D. and Pecknold, D. A. (1977), “Nonlinear biaxial stress-strain law for concrete”, *ASCE J. Eng. Mech. Division*, **103**(2): 229-241.
- Dong, Y.G. and Lu, X.L. (2007), “Study on axial compression ratio calculation and limit value for steel reinforced concrete walls”, *J. Earthq. Eng. Eng. Vib.*, **27**(1), 80-85.
- Duan, Y.F., He, K., Zhang, H.M., Ting, E.C., Wang, C.Y., Chen, S.K. and Wang, R.Z. (2014), “Entire-process simulation of earthquake-induced collapse of a mockup cable-stayed bridge by vector form intrinsic finite element (VFIFE) Method”, *Adv. Struct. Eng.*, **17**(3), 347-360. <https://doi.org/10.1260/1369-4332.17.3.347>.
- Duan, Y.F., Wang, S.M., Wang, R.Z., Wang, C.Y., Shih, J.Y., Yun, C.B. (2018), “Vector form intrinsic finite-element analysis for train and bridge dynamic interaction”, *J. Bridge Eng.*, **23**(1), [https://doi.org/10.1061/\(ASCE\)BE.1943-5592.0001171](https://doi.org/10.1061/(ASCE)BE.1943-5592.0001171).
- Duan, Y.F., Wang, S.M., Wang, R.Z., Wang, C.Y., and Ting, E.C. (2017), “Vector form intrinsic finite element based approach to simulate crack propagation”, *J. Mech.*, **33**(6), 1-16. <https://doi.org/10.1017/jmech.2017.85>.
- GB 50011-2010 (2010), Code for seismic design of buildings, Industry Standard of the People’s Republic of China; Beijing, China.
- Gulsan, M.E., Albegmpri, H.M. and Cevik, A. (2018), “Finite element and design code assessment of reinforced concrete haunched beams”, *Struct. Eng. Mech.*, **66**(4), 423-438. <https://doi.org/10.12989/sem.2018.66.4.423>.
- Hillerborg, A., Modeer, M., and Peterson, P.E. (1976), “Analysis of crack formation and crack growth in concrete by means of fracture mechanics and finite element”, *Cement Concrete Res.*, **6**(6):773-782. [https://doi.org/10.1016/0008-8846\(76\)90007-7](https://doi.org/10.1016/0008-8846(76)90007-7).
- Jiang, J.Q., Lu, X.Z., and Ye, L.P. (2005), *Finite Element Analysis of Concrete Structures*, Tsinghua University Press, Beijing, China.

- Kupfer, H. and Gerstle, K. (1973), "Behavior of Concrete under Biaxial Stress", *ASCE J. Eng. Mech. Division*, **66**(8), 853-866.
- Lefas, I.D., Kotsovos, M.D., Ambraseys, N.N. (1990), "Behavior of reinforced-concrete structural walls - strength, deformation characteristics, and failure mechanism", *ACI Struct. J.*, **87**(1), 23-31.
- Lu, Xilin, Zhang, Ying, Zhang, Hongmei, Zhang Hanshu. (2018), "Experimental study on seismic performance of steel fiber reinforced high strength concrete composite shear walls with different steel fiber volume fractions", *Eng. Struct.*, **171**(2018), 247-259. <https://doi.org/10.1016/j.engstruct.2018.05.068>.
- Luo, Y. Z. and Yang, C. (2014), "A vector-form hybrid particle-element method for modeling and nonlinear shell analysis of thin membranes exhibiting wrinkling", *J. Zhejiang University-Sci. A*, **15**(5), 331-350. <https://doi.org/10.1631/jzus.A1300248>.
- Mattiasson, K. (1981), "Numerical results from large deflection beam and frame problems analyzed by means of elliptic integrals", *J. Numerical Methods Eng.*, **17**(1), 145-153. <https://doi.org/10.1002/nme.1620170113>.
- Messaoudi, K., Boukhalfa, A. and Beldjelili, Y. (2018), "Three dimensional finite elements modeling of FGM plate bending using UMAT", *Struct. Eng. Mech.*, **66**(4), 487-494. <https://doi.org/10.12989/sem.2018.66.4.487>.
- Shih, C., Wang, Y.K. and Ting, E.C. (2004), "Fundamentals of a vector form intrinsic finite element: Part 3 Connected material frame and examples", *J. Mech.*, **20**(2), 133-143. <https://doi.org/10.1017/S172771910000335X>.
- Saenz, L. P. (1964), Discussion of "Equation for the stress-strain curve of concrete", *Proceeding of American Concrete Institute*. **61**, 1229-1235.
- Thomsen, J.H. and Wallace, J.W. (2004), "Displacement-based design of slender reinforced concrete structural walls—experimental verification", *J. Struct. Eng.*, **130**(4), 618-630. [https://doi.org/10.1061/\(ASCE\)0733-9445\(2004\)130:4\(618\)](https://doi.org/10.1061/(ASCE)0733-9445(2004)130:4(618)).
- Ting, E.C., Shih, C. and Wang, Y.K. (2004a), "Fundamentals of a vector form intrinsic finite element: Part 1 Basic procedure and a plane frame element", *J. Mech.*, **20**(2), 113-122. <https://doi.org/10.1017/S1727719100003336>.
- Ting, E.C., Shih, C. and Wang, Y.K. (2004b), "Fundamentals of a vector form intrinsic finite element: Part 2 Plane solid element", *J. Mech.*, **20**(2), 123-132. <https://doi.org/10.1017/S1727719100003348>.
- Ting, E.C., Wang, C.Y., Wu, T.Y., Wang, R.Z. and Chuang, C.C. (2006), "Motion analysis and vector form intrinsic finite element", Report No. CBER-2006-W-001, National Central University.
- Ting, E.C., Duan, Y.F and Wu, T.Y. (2012), *Vector mechanics of Structures*, Science Press, Beijing, China. (in Chinese).
- Wang, M.C., and Shao, M. (1997), *Basic Principles and Numerical Methods of Finite Element Method*, Tsinghua University Press, Beijing, China.
- Wu, T. Y. and Ting, E. C. (2008), "Large deflection analysis of 3d membrane structures by a 4-node quadrilateral intrinsic element", *Thin-Walled Struct.*, **46**(3), 261-275. <https://doi.org/10.1016/j.tws.2007.08.043>.
- Wu, T. Y., Wang, R. Z. and Wang, C. Y. (2006), "Large deflection analysis of flexible planar frames", *J. Chinese Institute Eng.*, **29**(4), 593-606. <https://doi.org/10.1080/02533839.2006.9671156>.
- Wang, R. Z., Tsai, K. C. and Lin, B. Z. (2011), "Extremely large displacement dynamic analysis of elastic-plastic plane frames", *Earthq. Eng. Struct. Dynam.*, **40**(13), 1515-1533. <https://doi.org/10.1002/eqe.1102>.
- Wu, T. Y. (2013), "Dynamic nonlinear analysis of shell structures using a vector form intrinsic finite element", *Eng. Struct.*, **56**(2013), 2028-2040. <https://doi.org/10.1016/j.engstruct.2013.08.009>.
- Yu, Y. and Luo, Y. Z. (2009a), "Motion analysis of deployable structures based on the rod hinge element by the finite particle method", *Proceedings*, **223**(7), 955-964. <https://doi.org/10.1243/09544100JAERO498>.
- Yu, Y. and Luo, Y. Z. (2009b), "Finite particle method for kinematically indeterminate bar assemblies", *J. Zhejiang University Sci. A*, **10**(5), 667-676. <https://doi.org/10.1631/jzus.A0820494>.
- Yang, C., Shen, Y. B. and Luo, Y. Z. (2014), "An efficient numerical shape analysis for light weight membrane structures", *J. Zhejiang University-Sci. A*, **15**(4), 255-271. <https://doi.org/10.1631/jzus.A1300245>.
- Zhang, H.M., Lu, X.L., Duan Y.F. and Zhu, Y. (2014), "Experimental study on failure mechanism of rc walls with different boundary elements under vertical and lateral loads", *Adv. Struct. Eng.*, **17**(3), 361-379. <https://doi.org/10.1260/2F1369-4332.17.3.361>.
- Zhang, H.M., Lu, X.L. and Wu X.H. (2010b), "Experimental study and numerical simulation of the reinforced concrete walls with different stirrup in the boundary element", *J. Asian Architecture and Build. Eng.*, **17**(2), 447-454. <https://doi.org/10.3130/jaabe.9.447>.
- Zhang, H.M., Lu, X.L. and Lu, L. (2007), "Influence of boundary element on seismic behavior of reinforced concrete shear walls", *J. Earthq. Eng. Eng. Vib.*, **27**(1), 92-98.
- Zhang, H.X., Liu, H. and Li, G.C. (2019), "Seismic performance of encased steel plate-reinforced gangue concrete composite shear walls", *KSCE J. Civil Eng.*, **23**(7), 2919-2932. <https://doi.org/10.1007/s12205-019-0286-9>.
- Zhu, B.L. and Dong, Z.X. (1985), *Nonlinear Analysis of Reinforced Concrete*, Tongji University Press, Shanghai, China. (in Chinese)

CC